Lattice spacing and multi-dimensional forces in the cross-bridge

C. David Williams[1]
Department of Physiology and Biophysics,
University of Washington, Seattle, Washington

Michael Regnier
Department of Bioengineering,
University of Washington, Seattle, Washington

Thomas L. Daniel
Department of Biology,
University of Washington, Seattle, Washington

[1]Corresponding Author. Email: cdave@uw.edu

Abstract

Existing mechanochemical models of muscle contraction treat myosin as a simple linear spring arranged parallel to the contractile filaments. These single-spring models cannot simulate the radial force that muscle generates (orthogonal to the direction of contraction) or the effects of altered filament lattice spacing. We describe a more complex myosin cross-bridge model that uses multiple springs to replicate myosin's force-generating power stroke and account for the effects of lattice spacing and radial force. The four springs which comprise this model (the 4sXB) correspond to the mechanically relevant portions of myosin's structure. As occurs *in vivo*, the 4sXB's state-transition kinetics and force production dynamics vary with lattice spacing.

Additionally, we describe a simpler two spring cross-bridge (2sXB) model which produces results similar to those of the 4sXB model. Unlike the 4sXB model, the 2sXB model requires no iterative techniques, making it more computationally efficient. The rate at which the multi-spring cross-bridges bind and generate force decreases as lattice spacing grows. Axial and radial forces generated by the 4sXB and 2sXB increase in magnitude as lattice spacing is offset from the myosin head resting position. Importantly, our results mirror those for intact, contracting muscle force production.

Keywords: cross-bridge model; cross-bridge kinetics; lattice spacing; radial force; muscle model; myosin

Introduction

Radial forces are of the same order as axial forces in contracting muscles (1–3). These forces, along with the radial lattice spacing of myofilaments, are thought to be key determinants of muscle force generation (4). At the same time, structural information about myosin cross-bridges suggests that force is generated through the action of a lever arm (5–7). That lever arm generates the strain accompanying the power stroke via a change in the rest angle at which the lever is attached to S1 region (7, 8). This change in angle occurs at the converter region, a flexible area which acts as a torsional spring. These phenomena may be related: the radial forces a cross-bridge generates are a result of the lever arm's geometry (9).

Existing theoretical and computational models of cross-bridge force generation, at the level of myofilaments, assume force is generated by a simple linear spring oriented parallel to the long axis of the myofilaments (Fig. 1B). This assumption has persisted from the earliest fundamental models of muscle contraction to more elaborate and spatially explicit models (10–14). These single-spring models have yielded insight into the processes that regulate production of force in the direction of contraction. However, these prior models of muscle contraction have paid less attention to radial forces and the effects of changes in filament lattice spacing. As a result, geometries of the single spring cross-bridge models have changed little while kinetic schemes governing transitions between conformational states have increased in complexity (10, 11, 15, 16). To analyze the radial forces that occur during muscle contraction, a different cross-bridge geometry is needed: a geometry that produces both forces aligned with and forces orthogonal to the direction of contraction. A lever arm made of several springs can simulate the deformations a cross-bridge undergoes as it generates force (the power stroke), can provide a geometry which is usable in cross-bridge models, and can account for both axial and radial forces (8).

Here we detail two models of cross-bridges that use multiple springs to replicate the lever arm mechanism and capture its biologically relevant effects. Both are affected by changes in lattice spacing and account for the radial component of force produced during the power stroke. The first model (referred to as the 4sXB model) simulates the cross-bridge as a system of four linearly elastic springs arranged in a geometry based upon the structure of the S1 and S2 regions of myosin II (Fig. 1D). Our second model (referred to as the 2sXB model) consists of two linearly elastic springs and provides greater computational efficiency than the 4sXB model while replicating many of the more complex model's behaviors (Fig. 1C). Both the 4sXB model and the 2sXB model use a three-state model of the cross-bridge cycle's kinetics, consisting of an unbound state, a low-force pre-power stroke state, and a force-producing post-power stroke state. The kinetics of transition from one state to another in our models are similar to those used previously but are generalized for use in two dimensions; our kinetics calculate transition probabilities using the free energy landscape of the cross-bridges instead of the offset of the cross-bridge head (Fig. 1A) (11, 13, 15, 17). We quantify both axial and the radial forces produced by our two cross-bridge models. Additionally, we explain how changes in lattice spacing affect kinetics and forces in our multiple-spring models.

Methods

Our two cross-bridge models, the 4sXB model and the 2sXB model (Fig. 1C-D), are designed to capture a range of mechanical behaviors observed or posited by prior work, namely radial force generation and the effects of lattice spacing on cross-bridge binding and force generation. Both cross-bridge models are an arrangement of linearly elastic torsional (angular) or Hookean (extensional) springs.

Geometry

Spring configurations To enable comparison with previous cross-bridge models, we implement a one-dimensional model in addition to our multi-spring models. This one-dimensional model uses a linearly elastic spring oriented parallel to the long axis of the thick filament (1sXB, Fig. 1B). The resulting cross-bridge forces are restricted to the direction of shortening, that is, axially oriented. The one-dimensional 1sXB model cannot yield radial forces. Moreover, this model's geometry is unable to account for kinetics or forces which depend on lattice spacing. This comparison model is identical to those used in recent spatially-explicit computational analyses (11–13).

The 4sXB model uses two linear and two torsional springs to represent the myosin head (Fig. 1D). This arrangement of four springs corresponds closely to regions of the cross-bridge believed to regulate and respond to strain or deformation (8). In particular, the four springs correspond to the point where the S2 region attaches to the rod, or α; the S2 region, or β; the point where the S2 region attaches to the light chain domain (LCD), or δ; and the LCD, or γ (Fig. 1D). Initial values and their sources are detailed in Table 1. The torsional spring δ is able to generate the force of the power stroke by a change in its rest angle, mimicking myosin's force generation by lever-arm (8, 18). Since the angle at which the head attaches to actin remains unchanged in our model, the torque generated at the converter region can be accounted for with a torsional spring on the end of LCD linear spring closer to the thick filament attachment point (18). By using a two-dimensional array of springs the 4sXB model allows us to compute radial forces and other cross-bridge properties that are not present in the 1sXB's one-dimensional space. To simulate the power stroke, the rest angle of the torsional spring linking the S2 domain and the LCD increases during the transition from a pre-power stroke to a post-power stroke state. This method of force generation acts in two dimensions and thus allows us to include the role lattice spacing plays in determining the forces and state transition rates of the cross-bridges.

The 2sXB model is a simplification of the 4sXB model and uses one linear spring (ρ); and one torsional spring (θ) to represent the myosin head (Fig. 1C). In the 2sXB model, there is still a lever arm mechanism generating force. Moreover, we adjusted the length of the 2sXB model's lever arm so that the distance from the thick filament to the tip of the cross-bridge is identical to the same measurement in the 4sXB model. The parameters characterizing the 2sXB model are chosen to match the step size, tip location and kinetics of the 4sXB model. Step size is the axial distance between a myosin head's pre- and post-power stroke positions when the head is not permitted to move in the radial direction, the distance by which the powerstroke changes the effective rest length of the cross-bridge. The result is computationally simpler than the 4sXB model, while retaining the 4sXB's two-dimensional behavior.

Parameters used in both cross-bridge models are derived, where possible, from existing experimental data, described below. Each linear spring (one in the 1sXB model, two in the 4sXB model and one in the 2sXB model) has a rest length and a spring constant, while each torsional spring (two in the 4sXB model and one in the 2sXB model) has a rest angle and a spring constant. The lengths and angles of the springs used for the 4sXB are based on tomographic reconstructions of *in vivo* S2 lengths and x-ray crystallographic reconstructions of the S1 fragment (5, 19). The rest length and angle of the springs used in the 2sXB model are set so that the tips of both the 2sXB's and 4sXB's simulated myosin heads are in the same location before and after the power stroke.

Calculation of lattice spacing Lattice spacing is given as d_{10}, the spacing between adjacent myosin lines, a measurement common in x-ray diffraction studies of muscle (3). We calculate d_{10} lattice spacing from both the geometry of the cross-bridge and the lattice spacing at which the cross-bridge generates the least radial force. The measurement of lattice spacing that the multi-spring cross-bridges provide is analogous to the *in vivo* surface-to-surface distance between the thick and thin filament faces. After simulations are complete, the d_{10} spacing is calculated from this surface-to-surface lattice spacing (ssLS) with a correction factor compensating for d_{10} being measured from the center of one thick filament to the center of another. Specifically, d_{10} is found from $d_{10} = 1.5(ssLS + cf)$ (3). The correction factor, cf, is used to set ssLS so that, at rest lattice spacing, the post-power stroke cross-bridge generates neither compressive nor tensile radial force. This offset becomes 6.90 nm when the rest d_{10} spacing is 34 nm (20). The ssLS that correspond to the d_{10} spacings of interest are then calculated and used to define the window of lattice spacings we examine (3). Thus the calculation of lattice spacing within the model is parametrized by resting ssLS, the lattice spacing at which radial forces are minimized, and the geometry of the actomyosin lattice.

Displacement and force generation Each cross-bridge undergoes a distortion as myosin hydrolyzes ATP to ADP.P_i; this distortion is the basis of the power stroke (11, 13, 15). The energy liberated by the hydrolysis of P_i drives force generation by inducing strain in the cross-bridge, appearing as a change in the cross-bridge's rest length (21). For the 1sXB model, this distortion is represented as a change in the rest length of the cross-bridge's only spring. The 4sXB and 2sXB models use a process which adheres more closely to the *in vivo* lever-arm mechanism; they represent the power stroke as a change in the rest angle of a torsional spring (22). The force generated by this process has both axial and radial components. The axial component of the force vector is the portion that lies along the long axes of the thick and thin filaments. The radial component of this vector lies perpendicular to the thick and thin filaments, orthogonal to the axial component. The relative values of the post-power stroke axial and radial forces are determined by the cross-bridge's construction (number of springs and their geometry), and the displacement of the cross-bridge tip from its rest position.

Calculation of spring lengths and angles To calculate the force and energy a cross-bridge produces and stores as its tip is displaced, we need to know the lengths and angles of the springs that constitute the cross-bridge. When the 1sXB model is placed under strain, its myosin head moves in the axial direction to a new horizontal offset from the thick filament attachment site at the cross-bridge's base. Finding the length of the 1sXB model's spring is simple, as it must span

the complete distance from the cross-bridge tip to the thick filament attachment site. Finding the lengths and angles of springs in the 4sXB and 2sXB models is a two-dimensional problem; they must account for both the axial and radial distances from cross-bridge tip to base. The values of the 2sXB model's springs may be determined analytically, as both spring values are set by the choice of a head location. The 2sXB model's spring values, ρ and θ, are given by $\rho(t_x, t_y) = (t_x^2 + t_y^2)^{1/2}$ and $\theta(t_x, t_y) = \arctan(t_y/t_x)$, for a cross-bridge tip location of (t_x, t_y) (Fig. 1C). The 4sXB model's greater number of springs give it another point whose location must be defined: (δ_x, δ_y), the S2/LCD linking point where the angular spring δ is located (Fig. 1D). The location of the δ spring cannot be analytically determined, it requires iterative optimization. We use a modification of Powell's "dog-leg" method (from Jones et al. (23)) to relax the location of the δ spring so that the 4sXB model is at its lowest energy state for the current cross-bridge tip position. Once δ's location is known, its angle, the angle of α and the lengths of β and γ are determined analytically. The angles and lengths for a given tip location (t_x, t_y) and δ location (δ_x, δ_y) are given by:

$$\begin{aligned}
\alpha(\delta_x, \delta_y) &= \arctan(\delta_y/\delta_x) \\
\beta(\delta_x, \delta_y) &= (\delta_x^2 + \delta_y^2)^{1/2} \\
\delta(\delta_x, \delta_y, t_x, t_y) &= \arctan((t_y - \delta_y)/(t_x - \delta_x)) + \pi - \alpha(\delta_x, \delta_y) \\
\gamma(\delta_x, \delta_y, t_x, t_y) &= ((t_x - \delta_x)^2 + (t_y - \delta_y)^2)^{1/2}
\end{aligned}$$

Kinetics

To describe the kinetics we use a simplified three-state model of the cross-bridge cycle (13, 15). This simplified system directly links the cross-bridge's kinetics and mechanics; the three kinetic states are directly comparable to the myosin configurations described in Houdusse et al. (18). The kinetic rates are independent of the number of springs used in a model cross-bridge, allowing the 4sXB and the 2sXB models to use the same system. The three states represented in our kinetics are (1) an unbound state: Myosin-ADP-P_i (2) a loosely-bound state:Actin-Myosin-ADP-P_i and (3) a force-generating post-power stroke state: Actin-Myosin-ADP (Fig. 1A).

The kinetics of both the 4sXB and the 2sXB models are strain dependent and are essentially transforms of the free energy landscapes experienced by the cross-bridges in their different states. These free energies are a function of the distortion necessary to move the point representing the simulated myosin head's tip to the point where we presume a binding site to be. Examples of these free energy landscapes are shown in Figure 2A and B, with cuts through them at the rest lattice spacing visible in Figure 3A.

The binding in both the 4sXB and the 2sXB models is determined by Monte-Carlo simulations of their diffusion as a result of being perturbed by Boltzmann-derived energy distributions (24). After a new head location is found, a binding probability is calculated which decreases exponentially with distance from the potential binding site. This probability is tested against a random number from a uniform distribution to determine if binding occurs in a given time step.

Free energy in each state The total free energy liberated by the hydrolysis of the gamma P_i of ATP and available to the myosin head over the course of a cross-bridge cycle (ΔG) depends

on both the standard free energy of ATP hydrolysis ($\Delta G_{0,ATP}$) and the concentrations of ATP, ADP and P_i. The free energy available to the cross-bridge over its cycle is given by $\Delta G = -\Delta G_{0,ATP} - \ln \frac{[ATP]}{[ADP][P_i]}$. Only a portion of the liberated free energy is available to the cross-bridge in a given state (13, 15). The limits on the amount of ΔG that can be used for mechanical work are included in the free energy of each state as an efficiency factor. The weakly bound state's efficiency is 28%, accounted for with $\alpha_e = 0.28$, and the strongly bound state's efficiency is 68%, accounted for with $\eta_e = 0.68$. The free energy of a cross-bridge in each state also depends on the strain the cross-bridge experiences from distortion upon binding. Thus the free energy of the cross-bridge in state i (U_i) is a linear combination of the strain-dependent and phosphate-dependent energy of the cross-bridge. The free energies of the 4sXB system are:

$$\begin{aligned}
U_1(\alpha,\beta,\delta,\gamma) &= 0 \\
U_2(\alpha,\beta,\delta,\gamma) &= \alpha_e \Delta G + \frac{k_\alpha(\alpha-\alpha_0)^2 + k_\beta(\beta-\beta_0)^2 + k_\delta(\delta-\delta_0)^2 + k_\gamma(\gamma-\gamma_0)^2}{2} \\
U_3(\alpha,\beta,\delta,\gamma) &= \eta_e \Delta G + \frac{k_\alpha(\alpha-\alpha_0)^2 + k_\beta(\beta-\beta_0)^2 + k_\delta(\delta-\delta_1)^2 + k_\gamma(\gamma-\gamma_0)^2}{2}
\end{aligned}$$

The free energies of the 2sXB system are:

$$\begin{aligned}
U_1(\theta,\rho) &= 0 \\
U_2(\theta,\rho) &= \alpha_e \Delta G + \frac{k_\rho(\rho-\rho_0)^2 + k_\theta(\theta-\theta_0)^2}{2} \\
U_3(\theta,\rho) &= \eta_e \Delta G + \frac{k_\rho(\rho-\rho_1)^2 + k_\theta(\theta-\theta_1)^2}{2}
\end{aligned}$$

Binding rate calculation Our binding algorithm follows Tanner et al. (13) but differs in two key ways: (1) we treat binding to the thin filament as a two step process and (2) our diffusion step works with any number of springs. Binding depends on diffusion of the cross-bridge head and proximity to the nearest binding site. Analogously, the process we use to simulate binding begins with the diffusion of the myosin head to a new location followed by possible attachment to the nearest binding site (depending on the distance from the head and the binding site). The diffusion step is simulated by thermally forcing each of a cross-bridge's constituent springs with an energy taken from a Boltzmann distribution (21, 25). This energy is used to calculate the deformation (change in length or angle) of each spring. Generating a diffusion energy and calculating the resulting offset of a spring is implemented as selecting a sample from the probability density function $P(x) = \sqrt{k/(2\pi kT)}\exp^{-(kx^2)/(2kT)}$ where x is the offset, k is the spring constant of the particular spring, and T is the system's temperature in Kelvin (21, 24). We find the updated location of the cross-bridge head from these new spring lengths and angles. The probability of cross-bridge attachment depends on the distance (d) from the cross-bridge head's new location to the nearest binding site: $p_{12}(d) = \tau \exp^d$, where τ is a scale factor chosen to provide attachment rates consistent with previous work (11, 13). Attachment occurs when p_{12} is greater, on a given time step, than a random number chosen from a uniform distribution in the domain 0 to 1 (13). Binding rates are calculated as the fraction of an ensemble of cross-bridges that bind given the same starting conditions. Thus, for an ensemble of size n:

$$r_{12} = \frac{\sum_0^n \left(1 \text{ if } \tau \exp^{-d} > rand, \text{ else } 0\right)}{n}$$

This two step system, with diffusion followed by a chance of attachment, is used for both the 4sXB and 2sXB models with only a change in the number of thermally forced springs.

Power stroke and detachment rates The power stroke and detachment rates are evolved from prior models (13, 15). In our power stroke and detachment rates, dependence on cross-bridge head distortion is replaced with a dependence on the free energy of the cross-bridge. These free energy dependent rates are insensitive to the number of springs composing a cross-bridge and function similarly in one- and two-dimensional models. Both the power stroke rate (r_{23}) and the detachment rate (r_{31}) depend on distortion, since they depend on the differences in free energy between the current state and the one being considered for transition. This dependence on the difference in free energies means transitions are more likely when they are energetically favorable and less likely in other circumstances, a natural scheme based in the geometry of the cross-bridges. The particular rates for both the 4sXB and the 2sXB models are:

$$r_{23}(U_2, U_3) = 100 + 100 \tanh(4 + 0.4(U_2 - U_3))$$

$$r_{31}(U_3, U_1) = 20 + 100(U_3 - U_1)^{1/2}$$

Calculation of reverse rates The reverse transition rate from state i to state j is given by the thermodynamically balancing formula $r_{ij}/r_{ji} = \exp^{U_i - U_j}$ where r_{ji} is the forward rate and r_{ij} is the reverse rate (11, 13, 15). The transition from a pre-power stroke state to an unbound state requires the reverse transition again be treated as a fraction of an ensemble of transition opportunities.

Results

The 4sXB and 2sXB models detailed here were developed to discover the consequences of lattice spacing on cross-bridge kinetics and two dimensional force production. Multi-spring cross-bridges introduce a lattice spacing dependence into force production and kinetics, and account for radial forces not aligned with the direction of contraction. As lattice spacing changes, the kinetics and forces of the 4sXB and 2sXB models shift in both magnitude and axial offset (the distance from where the S2/thick filament join to a property's extreme value or point of inflection).

At 34 nm d_{10}, the multi- and single-spring cross-bridges have similar kinetics and energies At rest lattice spacing, the free energies and kinetics of the of the single- and multi-spring cross-bridge models are largely similar, as seen in Figure 3 (where the 1sXB values used are calculated as in Tanner et al. (13, Fig. 10)). These properties are subject to the same trends because kinetics are conserved where possible between the multiple-spring and single-spring cross-bridges (15). The free energies of the multi-spring cross-bridges are a result of both extensional springs that are at an angle to the thick filament and angular springs sensitive to the angle they make with the thick filament. As the multi-spring cross-bridges are moved in the axial direction, the angles they make with the thick filament change. Thus the free energies of the multi-spring cross-bridges are skewed from the symmetric hyperbola of the 1sXB (Fig. 3A). The two-dimensional diffusion-based binding probability function that governs the multi-spring cross-bridges (as described in the binding

rate calculation section) causes their likely binding areas to occupy a greater range of axial positions than those of the single-spring cross-bridge (Fig. 3B) (24, 25). Multi-spring cross-bridges are thus less likely than the 1sXB model to bind at a small offset, but more likely to bind at larger offsets. This flattening and spreading of the binding probability function is a result of the extra degrees of freedom of motion in the two-dimensional models. The power stroke rates of the multi-spring cross-bridges are the same as those of the single-spring cross-bridge, with energy-dependent terms using the sum of the free energy of every spring comprising a cross-bridge (Fig. 3C). The detachment rate of the 1sXB explicitly relies on cross-bridge head position as well as energy. This position dependence was removed in adapting the 1sXB model's detachment rate for the multi-spring cross-bridges . The detachment rate thus loses the intentional asymmetry that the position term provided and retains only the asymmetry created by the spring geometries of the 2sXB and 4sXB models (Fig. 3D). Hence, the detachment rate, like the other cross-bridge properties, maintains the greatest similarity to the 1sXB model that is consistent with both embedding the cross-bridge in multiple dimensions and transitioning to kinetics based on the free energy of the cross-bridge.

Axial offsets of most cross-bridge properties decrease as lattice spacing increases The axial offset of a cross-bridge property is the distance from the thick filament attachment site to the property's extreme value or point of inflection at a given lattice spacing. As lattice spacing increases, the axial offsets of most of the multi-spring cross-bridges' kinetics and free energies grow smaller. An example of this change in axial offset is visible in Figure 2A and B where the lowest energy point the 4sXB or the 2sXB may reach at a lattice spacing of 32 nm d_{10} is more than 3 nm further from the cross-bridge's thick filament attachment point than the lowest energy point reachable at a lattice spacing of 38 nm d_{10}. This relationship between axial offset and lattice spacing changes the behavior of a cross-bridge as lattice spacing grows or shrinks. Since binding at a large axial offset is unlikely to occur at larger lattice spacings, forward biasing of binding is decreased as lattice spacing increases (Fig. 2C-D). Similarly, decreases in the axial offset of the power stroke rate's inflection point as lattice spacing increases causes the size of the power stroke to change with lattice spacing (Fig. 2E-F). The detachment rate in the 4sXB model is the only cross-bridge property where the axial offset does not decrease as lattice spacing increases (Fig. 2G). This exception is explained by the radially aligned post-power stroke orientation of γ, the 4sXB model's final linear spring. Combined, these effects reduce the axial force a cross-bridge generates at larger lattice spacings with implications for the sarcomere length dependence of force production and relaxation. These multi-spring cross-bridge models are the first to be capable of reproducing these lattice spacing dependent effects on force production.

Probability of a cross-bridge being bound decreases as lattice spacing diverges from rest The number of cross-bridges in a force generating state depends on lattice spacing. As lattice spacing diverges from its 34 nm d_{10} rest value, attachment rates at any axial location decrease while detachment rates at any axial location increase (Fig. 2C-D and 2G-H). These kinetic rates change with lattice spacing because the difference in free energy, on which they depend, increases with lattice spacing. Binding rates are dependent on the difference in free energy between the unbound state and the pre-power stroke state. Detachment rates are dependent on the difference in the free energy between the post-power stroke state and the unbound state. As above, the rest lattice spacing is defined by the radial offset at which a multi-spring cross-bridge is under no strain. Thus, as the lattice spacing increases or decreases from the point where bound cross-bridges are under

the least strain, the energy difference between a bound state and the zero-energy unbound state increases. This increase in energy makes the cross-bridge increasingly likely to transition to the unbound state and remain there (Fig. 2C-D and 2G-H). An example of this decrease in the likelihood of a cross-bridge remaining bound can be seen in the 4sXB model, where the slowest detachment rate is 20/sec at a lattice spacing of 34 nm d_{10} but rises to 260/sec at 38 nm d_{10} (Fig. 2G). When a model incorporates multiple cross-bridges, the dependence of kinetic rates on lattice spacing decreases the chance that a cross-bridge will generate force as lattice spacing increases. This decrease in the probability of a single cross-bridge generating force does not take into account the changes in myosin-head-to-binding-site distance that occur when cross-bridge models are embedded in a spatially explicit model. Spatially explicit effects, such as cross-bridge induced realignment of binding sites, may counter the decreased rates of binding and increased rates of detachment that accompany larger lattice spacings. As the power stroke rates depend on the difference between tanh of two parabolic energy profiles, their maximum and minimum probabilities of a cross-bridge undergoing a power stroke do not change with lattice spacing (Fig. 2E-F). Individual cross-bridges spend less time in a bound state as a result of these changes in their kinetics as lattice spacing diverges from its rest value.

Forces at a given axial offset increase with lattice spacing The axial and radial forces at a given axial offset increase as lattice spacing grows larger. The force a cross-bridge produces trends from initial negative values at compressed lattice spacings, to spacings where little force is produced, to very positive values at expanded lattice spacings (Fig. 4E-H). This effect competes with the decreased rate of binding and force generation that a multi-spring cross-bridge experiences at greater lattice spacings. At large lattice spacings few cross-bridges will generate force, but those that do will generate more force per cross-bridge. An increase in forces with lattice spacing is seen, for example, when the 4sXB model has a 10 nm axial offset and 35 nm d_{10} and gives half the axial and half the radial force as the same cross-bridge does at 38 nm d_{10} (Fig. 4E,G). Similarly, when the 2sXB model has a 12 nm axial offset and 35 nm d_{10} it gives about two thirds of the axial and radial forces as at 38 nm d_{10} (Fig. 4F,H). These energy landscapes also show that no lattice spacing that is free of radial force at all axial offsets. The radial force produced by a cross-bridge, even at rest lattice spacing, increases in magnitude as the cross-bridge tip moves away from its unstrained axial offset. This omnipresent radial force may influence the actions of other cross-bridges by propagating through the lattice of contractile filaments, even at low levels of contraction. While the forces of both the 4sXB model and the 2sXB model undergo similar trends of increasing forces with lattice spacings, the details of their force landscapes differ as a result of their different spring geometries (Fig. 4). At large lattice spacings, this greater force per cross-bridge is countered by the decreased probability a cross-bridge will generate force, an interaction requiring a model of the half-sarcomere using the 2sXB or 4sXB to evaluate throughly (26).

Radial forces are of the same order of magnitude as axial forces The radial and axial components of force, produced by a 4sXB model or 2sXB model moved from its rest position to an axial offset, are of the same order of magnitude (Fig.s 3E-F and 4A-D). The values of the axial and radial forces produced by the multiple-spring cross-bridge models at rest lattice spacing are compared to those produced by the single-spring cross-bridge model in Figure 3E-F. The relative values of the radial and axial forces are visualized as the angles of the force vectors in Figure 4A-D. Axial locations and lattice spacings with balanced axial and radial forces produce force vectors

which are neither vertical nor horizontal, but in some intermediate orientation. Most axial and radial offsets are populated by such vectors, particularly regions a cross-bridge would be most likely to occupy (unlikely regions are not shown in the vector plots). The few regions dominated by one force, notably some small offset positions in the 2sXB model (Fig. 4D), are dominated by radial forces. This presence of large radial forces suggests that, in all but the least strained locations at the smallest axial offsets, radial forces will be present in magnitudes comparable to those of axial forces.

Discussion

Our multi-spring cross-bridge model was developed to understand how axial and radial forces depend on myofilament lattice spacing. The 4sXB and 2sXB models show two key features that differ significantly from prior cross-bridge models: (1) the inclusion of torsional springs and lever-arm mechanisms reveals a dependence of step size on lattice spacing and (2) this lever-arm mechanism produces radial forces and axial forces of the same magnitude, a ratio similar to that observed experimentally (1, 2, 20). These cross-bridge models are the first to make such comparisons. Moreover, these dependencies of step size and binding likelihood on lattice spacing help explain measured changes in force generation with changes in lattice spacings (3).

Force generated by a multi-spring cross-bridge depends on lattice spacing A multi-spring cross-bridge's energy landscape, and the resulting force, depend on the cross-bridge's lattice spacing. At most locations, the forces a cross-bridge produces at a given axial offset increase as lattice spacing grows and strain on the cross-bridge increases (Fig. 4E-H). While this increased cross-bridge strain translates into greater axial and radial force per post-power stroke cross-bridge, the binding probability decreases as lattice spacing increases (Fig. 2C-D). The decrease in attachment rate at extreme lattice spacings, while power stroke rates remain unchanged (Fig. 2E-F), suggests lattice spacing influences muscle fiber force generation by altering the rate of cross-bridge attachment rather than the power stroke rate (26). How this decreasing number of bound, force generating, cross-bridges translates into less force as lattice spacing increases in the compliant sarcomere (and how closely this effect will match experimental results) will be determined by incorporating multi-spring cross-bridges into larger, spatially explicit models.

Multi-spring cross-bridge step size varies with lattice spacing The geometry of the 4sXB and 2sXB models dictates that a change in step size must accompany a change in lattice spacing. The distance subtended by a given angle will grow as the length of the sides of the angle increase. Step size changes with lattice spacing because the difference between the pre-power stroke and the post-power stroke cross-bridge angle does not vary with changes in lattice spacing while the change in the length of the lever arm does. This phenomenon is more pronounced in the 2sXB model, which lacks a second set of springs that partially compensate for lattice spacing changes, placing the full burden of bridging the thick and thin filaments on the lever-arm (Fig. 5). The 4sXB model possesses a set of springs between the lever-arm and the thick filament that also adjust with lattice spacing, allowing the location of the 4sXB model's lever-arm pivot point to change with lattice spacing and causing the 4sXB model's step size to depend less strongly on the magnitude of

changes in lattice spacing (Fig. 5). Whether this phenomena is present in physical cross-bridges is not known; most measurements of step size have been made in isolated in-vitro preparations which are unable to simulate a change in muscle lattice spacing (21, 27). This factor may alter the force generated at different lattice spacings and the proportion of cross-bridges remaining bound after completing a power stroke. Greater step size will increase the cross-bridge's strain and probability of detachment shortly after power stroke is completed.

The 2sXB model approximates the 4sXB model The energies, kinetics, and forces generated by the 2sXB model are not exact duplicates of those governing the 4sXB model, but instead are subject to the same governing trends (Figs. 2, 3 and 4). Mimicry of the 4sXB by the 2sXB is intentional, because the 2sXB is a computationally efficient alternative to the 4sXB. The energies, binding rates, and power stroke rates of the multi-spring cross-bridges are almost identical, while the rate of detachment is rotated by approximately 20° between the two systems due to differences in the way the post-power stroke position is achieved (Fig. 2). The greatest difference between the 4sXB model and the 2sXB model are apparent in the forces they generate; while the axial force generated by both cross-bridges depends on lattice spacing, the 2sXB's axial force is more steeply dependent on lattice spacing. This pattern is reversed for the radial forces generated by the cross-bridges, where the 2sXB model's radial force is more dependent on lattice spacing than that of the 4sXB model. In each of these cases, the forces generated by the multi-spring cross-bridges are subject to the same trend as lattice spacing or axial offset from the binding site increases. This similarity of forces between the 2sXB model and the 4sXB model, and the close agreement between the energies and kinetics of the two cross-bridge representations, lends support to use of the 2sXB in cases where the 4sXB would be require prohibitively computational resources. Substitution of the 2sXB model for the 4sXB model reduces the runtime of a simulation by two orders of magnitude and puts multi-spring cross-bridge simulations of the half-sarcomere within reach.

Large radial component of forces may influence lattice spacing in multi-filament models The 2sXB and 4sXB are the first models of the cross-bridge, suitable for use in larger spatially explicit simulations of the half sarcomere, capable of monitoring observed radial forces (1–3). The 4sXB and the 2sXB produce large radial forces of the same order of magnitude as the axial forces generated by a cross-bridge. Muscle fibers display these radial forces by resisting width changes as osmotic pressure is applied (1). Direct measurement of lattice spacing by X-ray diffraction confirms fiber width estimates of radial force (28). Observations of lattice spacing during redevelopment of tension following length changes provides further experimental evidence of large radial forces (2). A spatially explicit model, even one using multiple thick and thin filaments arranged in a lattice, is insensitive to lattice spacing if it uses a version of the 1sXB model. Embedding multi-spring cross-bridges in a multi-filament model allows the simulation of radial force regulation in a lattice of thick and thin filaments. Radial force is a potential regulator of lattice spacing and of Ca^{2+} sensitivity as lattice spacing and sarcomere length vary (3). A multi-filament model using the 4sXB or 2sXB can simulate the interaction of radial force generated by a cross-bridge with radial forces provided by other mechanisms, e.g. titin or electrostatic repulsion (3, 26, 29). Thus multi-spring cross-bridges make it possible to evaluate the influence of these radial forces, posited to be regulators of lattice spacing, and processes which may depend on lattice spacing or myosin head to thin filament distance, such at the Frank-Starling mechanism; something not possible with a 1sXB model (30).

References

1. Maughan, D. W., and R. E. Godt, 1981. Radial forces within muscle fibers in rigor. *J Gen Physiol* 77:49–64.

2. Cecchi, G., M. A. Bagni, P. J. Griffiths, C. C. Ashley, and Y. Maeda, 1990. Detection of radial crossbridge force by lattice spacing changes in intact single muscle fibers. *Science* 250:1409–11.

3. Millman, B. M., 1998. The filament lattice of striated muscle. *Physiol Rev* 78:359–91.

4. Fuchs, F., and D. A. Martyn, 2005. Length-dependent Ca^{2+} activation in cardiac muscle: some remaining questions. *J Muscle Res Cell Motil* 26:199–212.

5. Rayment, I., W. Rypniewski, K. Schmidt-Bäse, R. Smith, D. Tomchick, M. M. Benning, D. Winkelmann, G. Wesenberg, and H. Holden, 1993. Three-Dimensional Structure of Myosin Subfragment-1: A Molecular Motor. *Science* 261:50–58.

6. Uyeda, T. Q. P., P. D. Abramson, and J. A. Spudich, 1996. The neck region of the myosin motor domain acts as a lever arm to generate movement. *Proc Natl Acad Sci USA* 93:4459–64.

7. Huxley, A. F., 2000. Mechanics and models of the myosin motor. *Philos Trans R Soc Lond, B, Biol Sci* 355:433–40.

8. Houdusse, A., and H. L. Sweeney, 2001. Myosin motors: missing structures and hidden springs. *Curr Opin Struct Biol* 11:182–94.

9. Schoenberg, M., 1980. Geometrical factors influencing muscle force development. II. Radial forces. *Biophys J* 30:69–77.

10. Huxley, A. F., 1957. Muscle structure and theories of contraction. *Progress in biophysics and biophysical chemistry* 7:255–318.

11. Daniel, T. L., A. C. Trimble, and P. B. Chase, 1998. Compliant realignment of binding sites in muscle: transient behavior and mechanical tuning. *Biophys J* 74:1611–21.

12. Chase, P. B., J. M. Macpherson, and T. L. Daniel, 2004. A spatially explicit nanomechanical model of the half-sarcomere: myofilament compliance affects Ca^{2+}-activation. *Annals of biomedical engineering* 32:1559–68.

13. Tanner, B. C. W., T. L. Daniel, and M. Regnier, 2007. Sarcomere lattice geometry influences cooperative myosin binding in muscle. *PLoS Comput Biol* 3:e115.

14. Campbell, K. S., 2009. Interactions between connected half-sarcomeres produce emergent mechanical behavior in a mathematical model of muscle. *PLoS Comput Biol* 5:e1000560.

15. Pate, E., and R. Cooke, 1989. A model of crossbridge action: the effects of ATP, ADP and P_i. *J Muscle Res Cell Motil* 10:181–96.

16. Smith, D., M. A. Geeves, J. Sleep, and S. M. Mijailovich, 2008. Towards a Unified Theory of Muscle Contraction. I: Foundations. *Annals of biomedical engineering* 36:1624–40.

17. Takagi, Y., H. Shuman, and Y. E. Goldman, 2004. Coupling between phosphate release and force generation in muscle actomyosin. *Philos Trans R Soc Lond, B, Biol Sci* 359:1913–20.

18. Houdusse, A., A. G. Szent-Gyorgyi, and C. Cohen, 2000. Three conformational states of scallop myosin S1. *Proc Natl Acad Sci USA* 97:11238–43.

19. Taylor, K. A., H. Schmitz, M. C. Reedy, Y. E. Goldman, C. Franzini-Armstrong, H. Sasaki, R. T. Tregear, K. Poole, C. Lucaveche, R. J. Edwards, L. F. Chen, H. Winkler, and M. K. Reedy, 1999. Tomographic 3D reconstruction of quick-frozen, Ca^{2+}-activated contracting insect flight muscle. *Cell* 99:421–31.

20. Brenner, B., and L. C. Yu, 1991. Characterization of radial force and radial stiffness in Ca^{2+}-activated skinned fibres of the rabbit psoas muscle. *J Physiol* 441:703–18.

21. Howard, J., 2001. Mechanics of Motor Proteins and the Cytoskeleton. Sinauer Associates.

22. Reedy, M. C., 2000. Visualizing myosin's power stroke in muscle contraction. *J Cell Sci* 113:3551–62.

23. Jones, E., T. Oliphant, and P. Peterson, 2001. SciPy: Open source scientific tools for Python. `http://www.scipy.org/`.

24. Dill, K. A., and S. Bromberg, 2003. Molecular Driving Forces. Garland Science.

25. Berg, H. C., 1993. Random Walks in Biology. Princeton University Press.

26. Martyn, D. A., B. B. Adhikari, M. Regnier, J. Gu, S. Xu, and L. C. Yu, 2004. Response of equatorial x-ray reflections and stiffness to altered sarcomere length and myofilament lattice spacing in relaxed skinned cardiac muscle. *Biophys J* 86:1002–11.

27. Peterman, E. J. G., H. Sosa, and W. E. Moerner, 2004. Single-molecule fluorescence spectroscopy and microscopy of biomolecular motors. *Annu Rev Phys Chem* 55:79–96.

28. Matsubara, I., Y. E. Goldman, and R. Simmons, 1984. Changes in the lateral filament spacing of skinned muscle fibres when cross-bridges attach. *J Mol Biol* 173:15–33.

29. Cazorla, O., Y. Wu, T. C. Irving, and H. Granzier, 2001. Titin-based modulation of calcium sensitivity of active tension in mouse skinned cardiac myocytes. *Circ Res* 88:1028–35.

30. Smith, L., C. Tainter, M. Regnier, and D. A. Martyn, 2009. Cooperative cross-bridge activation of thin filaments contributes to the Frank-Starling mechanism in cardiac muscle. *Biophys J* 96:3692–702.

31. Liu, J., S. Wu, M. C. Reedy, H. Winkler, C. Lucaveche, Y. Cheng, M. K. Reedy, and K. A. Taylor, 2006. Electron tomography of swollen rigor fibers of insect flight muscle reveals a short and variably angled S2 domain. *J Mol Biol* 362:844–60.

32. Davis, J. S., and N. D. Epstein, 2009. Mechanistic role of movement and strain sensitivity in muscle contraction. *Proc Natl Acad Sci USA* 106:6140–5.

33. Gourinath, S., D. M. Himmel, J. H. Brown, L. Reshetnikova, A. G. Szent-Gyorgyi, and C. Cohen, 2003. Crystal structure of scallop Myosin s1 in the pre-power stroke state to 2.6 a resolution: flexibility and function in the head. *Structure* 11:1621–7.

34. Delano, W. L., 2008. The PyMOL Molecular Graphics System. DeLano Scientific, Palo Alto, CA, USA. `http://www.pymol.org`.

Tables

4sXB			
	Rest value	E	Source
α	40°	100 pN/rad	Liu et al. (31)
β	10.5 nm	10 pN/nm	Liu et al. (31)
δ	125°	40 pN/rad	Taylor et al. (19)
δ'	70°	40 pN/rad	Taylor et al. (19)
γ	9.6 nm	5 pN/nm	Houdusse et al. (18)
2sXB			
	Rest value	E	Source
θ	47°	40 pN/rad	See caption
θ'	73°	40 pN/rad	See caption
ρ	20 nm	2 pN/nm	See caption
ρ'	16 nm	2 pN/nm	See caption

Table 1: **Model parameters and their sources** Prime values, such as δ', represent post-power stroke state values. From Liu et al. (31), which used insect flight muscle, the most frequently occurring thick filament to S2 angle range is 51-60° . We assume that this range is being distorted by the compressive radial force being generated by the rigor cross-bridges in the swollen lattice spacings that Liu et al. (31) used. As such, we choose a rest angle for α at the low end of the still common range of 50° to 40° . We do not change this angle between states one, two and three. In Taylor et al. (19) (clearly explained in Davis and Epstein (32)) the angle between the LCD and the thick filament's axial axis goes from 125° to 70° with the power stroke. The LCD rest length generated by measurements made of structure 1DFK from Houdusse et al. (18). The rest values of the 2sXB model's springs are determined by those of the 4sXB model; they are calculated so that the rest position of the 2sXB's head is the same as the rest position of the 4sXB's head. The spring constant, E, for the angular spring responsible for each cross-bridge's power stroke is determined by the change in angle over the power stroke and the energy liberated by the hydrolysis of ATP (13). Additional spring constants are chosen to be consistent with previous work, and to provide sufficient flexibility to enable diffusion.

Figure Legends

Figure 1

Kinetics and cross-bridge types. (A) The three state kinetic system. The three states represent (1) an unbound state, (2) a pre-power stroke state, and (3) a post-power stroke state. The rate of transition between states i and j is represented as r_{ij}. The forward and reverse transition rates are functions of energy stored in the cross-bridge. (B)–(D) The three cross-bridge models, plotted against a myosin crystal structure for comparison (structure image generated from Gourinath et al. (33) with PyMol (34)). The energy landscape of each cross-bridge and the free energy at rest lattice spacing are shown adjacent to the cross-bridge schematic. (B) The 1sXB introduced in (10). (C) The 2sXB which uses a torsional/angular spring (θ) and a linear spring (ρ). (D) The 4sXB with two torsional and two linear springs. Of the 4sXB's springs, α corresponds to the point at which the S2 region rejoins the thick filament backbone, β to the S2 region itself, γ to the area linking the S2 and the light chain domains, and δ to the light chain domain itself. It is γ that replicates the change in angle accompanying the powerstroke.

Figure 2

Energy and kinetics of the multi-spring cross-bridge models as a result of changes to axial offset and lattice spacing. Axial offset is the distance between the current axial location of the cross-bridge's tip and the location where the cross-bridge attaches to the thick filament. Lattice spacing (d_{10}) is defined as in Millman (3), with an offset to account for filament thicknesses so the cross-bridge spans the filaments at a rest lattice spacing of 34 nm. (A)–(H) The properties of the 4sXB model (A, C, E, and G) and the 2sXB model (B, D, F, and H) as they change with binding site offset and lattice spacing. (A) depicts the free energy of the 4sXB model at various lattice spacings, with the head stretched to an axial offset from the thick filament attachment point. The free energy of the 2sXB model is shown in (B). (C) and (D) show r_{12}, the probability that the 4sXB and 2sXB models will transition from an unbound state to a bound state. (E) and (F) show r_{23}, the probability of transition from a pre-power stroke state to a post-power stroke state, for the same cross-bridges, axes, and scales as (C) and (D) show r_{12}. (G) and (H) show r_{31}, the probability of unbinding from a post-power stroke state. The reverse rates, r_{21}, r_{32}, and r_{13} are back-calculated from the forward rates.

Figure 3

Forces, energy, and kinetics of the 1sXB, 2sXB, and 4sXB models at resting lattice spacing. (A)–(F) show the energy, transition rates, and forces of the 1sXB model (black), 2sXB model (green), and 4sXB model (red) at resting lattice spacing. The 1sXB model values shown for comparison are derived from those of Daniel et al. (11) and Tanner et al. (13), shifted axially so the resting location of the cross-bridge head in each case is aligned with the resting locations of the 2sXB model and 4sXB model allowing easier comparison. The free energy of the cross-bridges in state two is shown in (A), where the multi-spring cross-bridges' shifts from a strictly parabolic

trajectory is visible. The explicit two-dimensional thermal forcing of the multi-spring cross-bridge heads in (B) results in binding probabilities that are more distributed than those of the single spring cross-bridge. The rate of power strokes (C) remains least changed between the single and the multi-spring cross-bridge models. The energy-based kinetics of the multi-spring cross-bridges are unable to fully replicate the biased detachment rate of the 1sXB model in (D). (E) and (F) show the 1sXB's sharp discontinuities in axial force and lack of any radial force.

Figure 4

Overview and detail of the forces exerted by the 2sXB and 4sXB models. (A)–(D) show the forces exerted by the 4sXB and the 2sXB models; omitted are vectors for unlikely configurations as determined by the sum of r_{23} and the inverse of r_{31}. (A) and (B) show overviews of the forces exerted, respectively, by the 4sXB model and the 2sXB model over lattice spacings and axial offsets that vary as in Figure 2. The forces exerted by the two cross-bridges have radial components which frequently equal or exceed their axial components. A more detailed view of the region surrounding the rest position of the cross-bridges is shown in (C) and (D), where the large radial components of the cross-bridge forces, particularly for the 2sXB model, is again evident. (E)–(H) show, separated, the axial and radial components of the 4sXB and the 2sXB models.

Figure 5

Changes in step size with lattice spacing. Step size varies as lattice spacing diverges from its rest value. Step size is defined as the change in the rest axial offset between the pre- and post-power stroke states. The 4sXB model and 2sXB model exhibit different tuning curves.

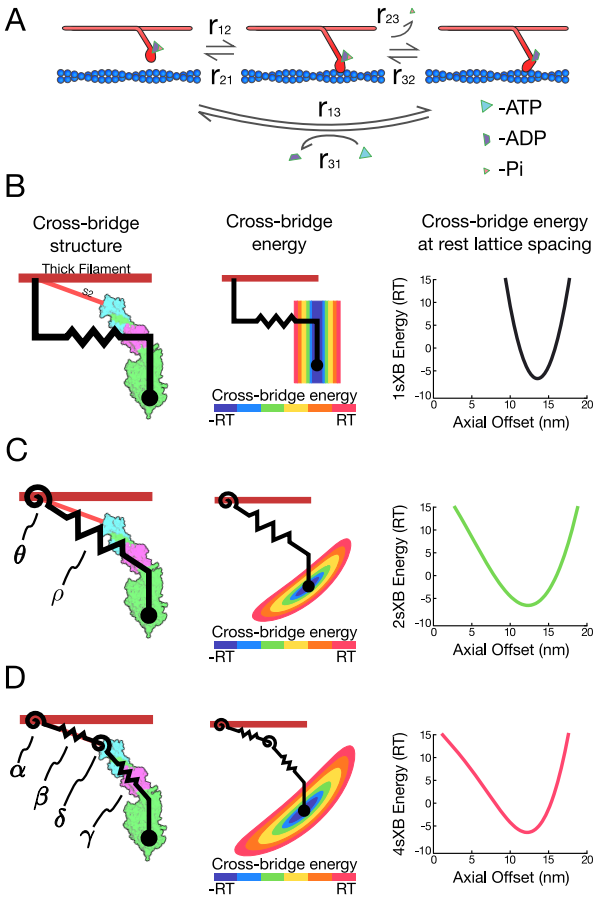
A
r12
r21
r23
r32
r13
r31
-ATP
-ADP
-Pi
B
Cross-bridge structure
Thick Filament
Cross-bridge energy
Cross-bridge energy
-RT
RT
Cross-bridge energy at rest lattice spacing
1sXB Energy (RT)
Axial Offset (nm)
C
θ
ρ
Cross-bridge energy
-RT
RT
2sXB Energy (RT)
Axial Offset (nm)
D
α
β
δ
γ
Cross-bridge energy
-RT
RT
4sXB Energy (RT)
Axial Offset (nm)

Figure 1:

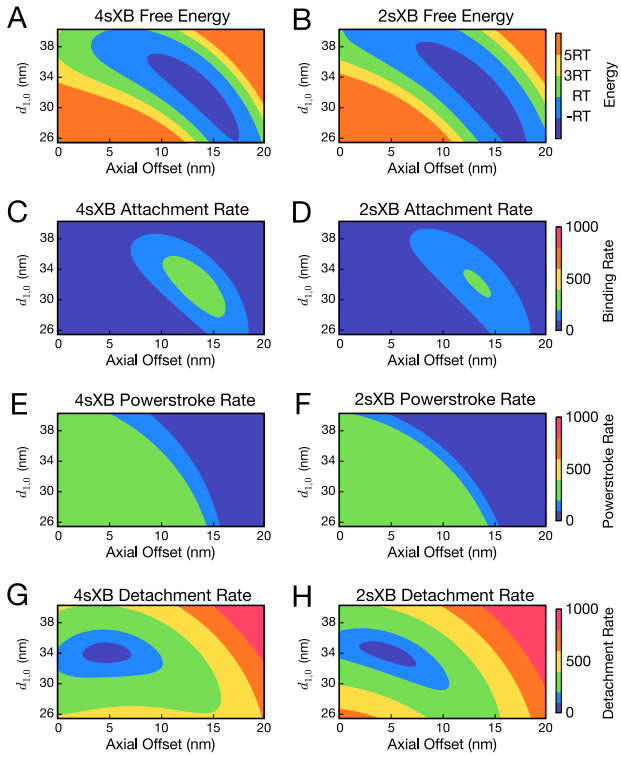
A
4sXB Free Energy
B
2sXB Free Energy
5RT
3RT
RT
-RT
Energy
C
4sXB Attachment Rate
D
2sXB Attachment Rate
1000
500
0
Binding Rate
E
4sXB Powerstroke Rate
F
2sXB Powerstroke Rate
Powerstroke Rate
G
4sXB Detachment Rate
H
2sXB Detachment Rate
Detachment Rate
$d_{1,0}$ (nm)
Axial Offset (nm)

Figure 2:

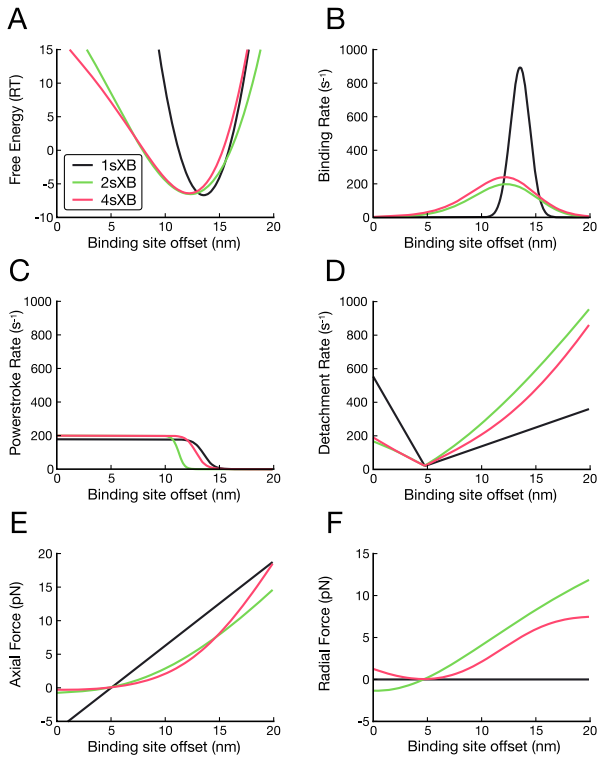
A
Free Energy (RT)
1sXB
2sXB
4sXB
Binding site offset (nm)
B
Binding Rate (s⁻¹)
Binding site offset (nm)
C
Powerstroke Rate (s⁻¹)
Binding site offset (nm)
D
Detachment Rate (s⁻¹)
Binding site offset (nm)
E
Axial Force (pN)
Binding site offset (nm)
F
Radial Force (pN)
Binding site offset (nm)

Figure 3:

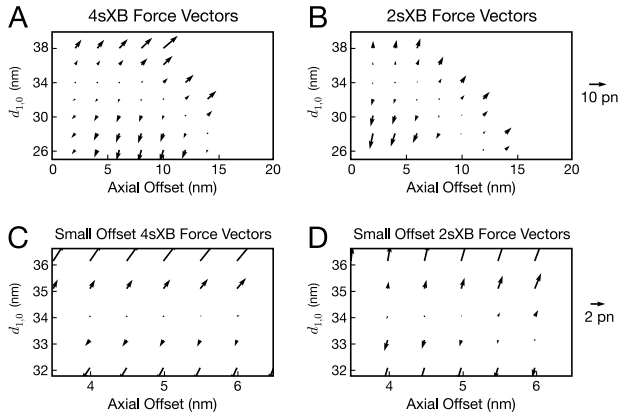
A
4sXB Force Vectors
B
2sXB Force Vectors
10 pn
C
Small Offset 4sXB Force Vectors
D
Small Offset 2sXB Force Vectors
2 pn
$d_{1,0}$ (nm)
Axial Offset (nm)

Figure 4:

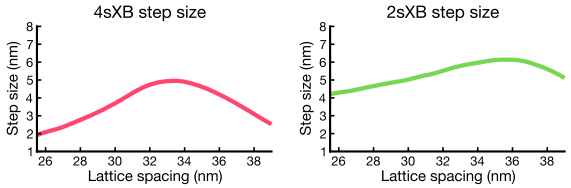
4sXB step size
Step size (nm)
Lattice spacing (nm)
2sXB step size
Step size (nm)
Lattice spacing (nm)

Figure 5: